ARL-TR-9028 • AUG 2020

Parametric Study of Dumbbell-Shaped Specimens for Compression Testing of Ceramics Using Finite Element Analysis

by Adam Taylor and John Pittari

NOTICES

Disclaimers

ARL-TR-9028 ● AUG 2020

Parametric Study of Dumbbell-Shaped Specimens for Compression Testing of Ceramics Using Finite Element Analysis

John Pittari
Weapons and Materials Research Directorate, CCDC Army Research Laboratory

Adam Taylor
College Qualified Leaders Program, Drexel University

REPORT DOCUMENTATION PAGE	*Form Approved* *OMB No. 0704-0188*

1. REPORT DATE *(DD-MM-YYYY)*	**2. REPORT TYPE**	**3. DATES COVERED (From - To)**
August 2020	Technical Report	30 March–18 September 2020

4. TITLE AND SUBTITLE

Parametric Study of Dumbbell-Shaped Specimens for Compression Testing of Ceramics Using Finite Element Analysis

5a. CONTRACT NUMBER

5b. GRANT NUMBER

5c. PROGRAM ELEMENT NUMBER

6. AUTHOR(S)

Adam Taylor and John Pittari

5d. PROJECT NUMBER

5e. TASK NUMBER

5f. WORK UNIT NUMBER

7. PERFORMING ORGANIZATION NAME(S) AND ADDRESS(ES)

CCDC Army Research Laboratory
ATTN: FCDD-RLW-MB
Aberdeen Proving Ground, MD 21005

8. PERFORMING ORGANIZATION REPORT NUMBER

ARL-TR-9028

9. SPONSORING/MONITORING AGENCY NAME(S) AND ADDRESS(ES)

College Qualified Leaders, Drexel University

10. SPONSOR/MONITOR'S ACRONYM(S)

11. SPONSOR/MONITOR'S REPORT NUMBER(S)

12. DISTRIBUTION/AVAILABILITY STATEMENT

Approved for public release; distribution is unlimited.

13. SUPPLEMENTARY NOTES

ORCID ID: John Pittari, 0000-0001-9611-3138

14. ABSTRACT

Compression strength testing of ceramics has historically been conducted using cylindrical- or cuboidal-shaped specimens due to simplistic analysis and reduced machining costs. However, these specimen geometries tend to exhibit large amounts of scatter and often fail from a nonuniform state of stress, rendering the strength results inconclusive. Instead, a dumbbell-shaped compression specimen has been proposed, simulated, and utilized for such strength tests to provide better estimates of material performance. This study reevaluates that specimen geometry via a modern finite element analysis simulation software. A parametric study is performed to investigate how modifications to the original specimen, its associated geometry, and simulation parameters could alter its performance during compression strength tests. High-rate testing with this specimen is also simulated using an explicit analysis code. It was determined that alterations to the specimen geometry most affected the performance, and it is suggested that a systematic study be carried out to identify further improvements to specimen geometry.

15. SUBJECT TERMS

ceramics, compression testing, finite element analysis, specimen geometry, stress concentration

16. SECURITY CLASSIFICATION OF:			**17. LIMITATION OF ABSTRACT**	**18. NUMBER OF PAGES**	**19a. NAME OF RESPONSIBLE PERSON**
a. REPORT	**b. ABSTRACT**	**c. THIS PAGE**			John Pittari
Unclassified	Unclassified	Unclassified	UU	35	**19b. TELEPHONE NUMBER (Include area code)** (410) 306-0773

Contents

List of Figures

List of Tables

1. Introduction

The evaluation of a ceramic's material properties via compression testing has for a long time been conducted using cylindrical or cuboidal specimens. However, during testing, specimens of cylindrical or cuboidal shape typically exhibit stress concentrations at the interface between specimen and the loading platen, causing them to fail prematurely, and in a nonuniform manner, leading to underestimated material performance.[1–3] In the 1980s, a dumbbell-shaped specimen was proposed to minimize these stress concentrations and produce more accurate values of material properties.[4,5] There had been some historical precedent investigating the potential advantages of using a dumbbell-shaped specimen for these types of tests.[1,6,7] Since then, several researchers have studied the behavior of dumbbell specimens, both computationally and experimentally, with varying loading conditions and made comparisons to other similar studies as well as tests using cylindrical and cuboidal specimens.[8–13] Their results show high reproducibility of material properties using a dumbbell specimen as well as highlight the pitfalls in using cuboidal or cylindrical specimens for determining material performance. This study attempts to validate the dumbbell design, as proposed by Tracy[4] and used by Dunlay et al.[8] for both simulations and experiments, and identify the effects of making modifications to the specimen and testing configuration. Computer simulations using a finite element analysis (FEA) code will be performed to test the bounds of each input parameter of a typical dumbbell compression test. The specific design features considered during a dumbbell compression test were separated into five studies to be evaluated parametrically:

1) Effect of scaling the specimen (Configurations A–C)
2) Effect of changing displacement rate (Configuration D)
3) Modification of specimen geometry (Configurations E–I)
4) Modification of the boundary conditions (Configurations J–L)
5) Effect of high-rate loading (Configuration M)

The first four studies were limited to quasi-static (QS) testing to isolate issues associated with explicit modelling of dynamic tests. The last study examined the effect of high-rate loading on performance of the dumbbell specimen. This was performed because ceramic materials are known to exhibit rate sensitivity when experiments are performed across a range of strain rates. Several of the aforementioned studies have investigated the use of dumbbell-shaped specimens for evaluating high-rate properties using split-Hopkinson pressure bar apparatuses, further supporting the final study.[9,11–15]

Each study parametrically changes an input variable during the setup of a compression test to evaluate the dominant features in design. For example, changing the overall size or shape of the dumbbell specimen may more substantially affect its performance than changing the displacement rate or configuration of the loading interface. A distinction like this could reduce the resources spent on enhancing the precision of the loading interface and allow more resources to be allocated on perfecting specimen geometry.

One consideration noticed during the analysis of dumbbell compression testing was the presence of a stress concentration located just outside of the gage section along the first fillet.[8] Quantifying the severity of each configuration's stress concentration at this location is desirable and is used to evaluate the performance of each configuration. More specifically, the magnitude of the axial (or compressive) stress and the cross-sectional area at that location during the onset of failure is calculated for each configuration. The values obtained from this region of maximum stress will then be compared to that of the gage section. The configuration that produces minimal differences in compressive stress and cross-sectional area between these two locations will provide the most accurate measurement of material properties during physical compression tests.

2. Modeling Procedure

2.1 Generation of FEA Model

Each dumbbell specimen and respective testing configuration was simulated using ANSYS, a finite element modeling and simulation software. The first step in simulating a compression test involved recreating the dumbbell size B specimen geometry from Dunlay[8], which will henceforth be referred to as the baseline configuration (Fig. 1).

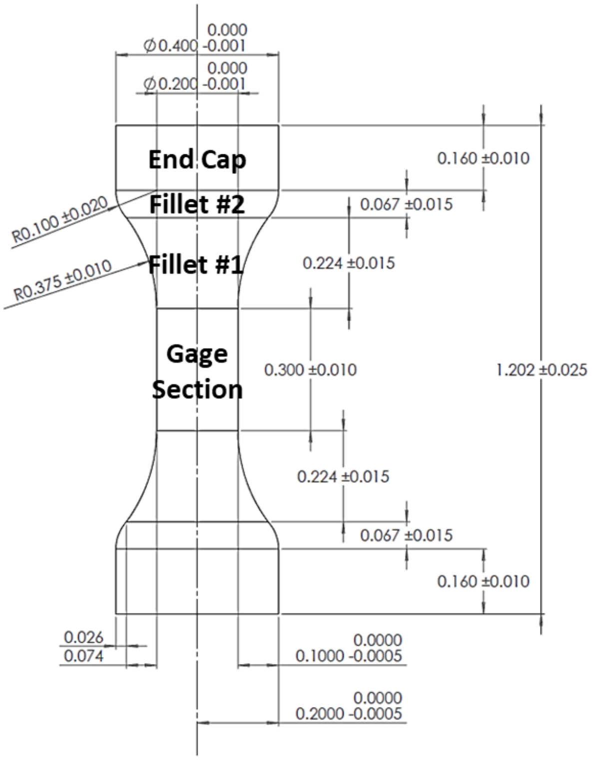

Fig. 1 Drawing of the dumbbell-shaped B size specimen geometry prescribed in Dunlay et al.[8] with noted geometric features of importance. This geometry was used to create the baseline specimen. Units are in inches.

ANSYS was used to create this baseline specimen geometry in addition to the other geometries evaluated in subsequent studies. Each specimen's geometry was modeled in 2D and consisted only of the upper-right quadrant of the specimen (seen in Fig. 2) to facilitate the use of an axisymmetric solver. The axisymmetric solver simulates 3D effects while allowing a greater resolution of elements on the 2D plane. Before inputting boundary conditions and external loads, a grid mesh was generated for each model (Fig. 2). Default settings were mostly used to calculate these meshes; however, the element size was reduced to 100 µm (0.004 inch) for better resolution, and the mesh was calculated using a "face meshing" scheme. Each configuration used this mesh geometry.

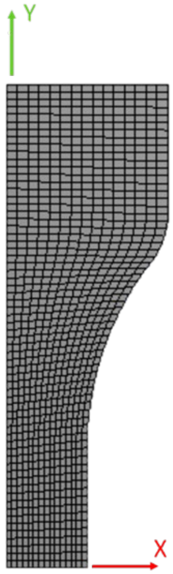

Fig. 2 The baseline 2D axisymmetric mesh geometry. The outline of the mesh was removed from every subsequent figure for aesthetic reasons.

Next, a "static structural" (i.e., QS) analysis was conducted for Configurations A–L. Two displacement constraints were placed on each specimen: one on the top that displaced the specimen at 0.25 mm/min, consistent with the crosshead displacement rate used for compression experiments in Dunlay[8], while restricting movement in the x-direction (assuming infinite friction per Dunlay[8]), and another on the bottom (midpoint of the full specimen) that restricted movement only in the y-direction (rolling support). For Configurations J and K, a tungsten carbide (WC) platen was instead displaced (at the same provided displacement rate) adjacent to the specimen's end caps to investigate the effect of a loading platen on the stress distribution at the interface with the specimen. The material properties for the WC insert can be found in Table 1, which were extracted from the same properties for the WC inserts used in Dunlay[8]. For Configuration L, a frictionless boundary condition was added to the top of the specimen to evaluate the effect of friction on dumbbell performance.

Table 1 Material properties used for the simulations

Property	**CAP3-Al_2O_3[16]**	**WC Insert[a] [8]**
Density (kg/m^3)	3900	14700
Young's modulus (GPa)	370	600
Poisson's ratio	0.22	0.28
Bulk modulus (GPa)	220	450
Shear modulus (GPa)	152	230

[a] Kennametal Grade K3406 (WC-7.8%Co)

An explicit dynamic test was also simulated using ANSYS's simulation software. Configuration M's geometry (the same as the baseline) was imported into the new solver with identical parameters to the baseline model. However, a displacement rate of 12 m/s, an approximation of the experimentally reached particle velocity during a high-rate compression test, such as in a split-Hopkinson pressure (a.k.a. Kolsky) bar experiment, was applied to the top edge of the end cap. A displacement condition was again placed on the bottom (midpoint of the full specimen) to restrict movement in the y-direction. The velocity was ramped to simulate the use of a pulse shaper (i.e., a constant velocity of 12 m/s was reached 250 µs into testing), but failure occurred well before this plateau value was reached.

2.2 Application of Material Parameters

The final step before executing the model was to apply a set of material parameters/properties to the geometry. The original studies both investigated an older vintage of alumina with 94% purity, Coors Porcelain Company's (now called CoorsTek) AD-94.[4,8] The same company has a more modern alumina with higher purity (99.5%) that is also considered their "armor-grade" version, Ceramic Armor Process 3 (CAP3). This is a material of special interest to the Army and has a similar non-armor grade version, AD-995, that has been extensively studied in literature. The material properties obtained from the manufacturer were used in this study and can be found in Table 1 along with the properties for the WC insert, taken from Dunlay[8], described previously.

In ANSYS, each specimen was loaded up to its experimentally derived compressive strength from the testing of the dumbbell-shaped specimen, as no fracture mechanics were applied in these simulations to determine failure. Therefore, the failure strength observed in the QS compression tests of Dunlay[8], 4.0 GPa, was used as the point of failure for studies 1–4. For dynamic testing, the upper limit of the compressive failure strength observed in Swab and Quinn,[10] 4.9 GPa, was used for Study 5.

When this failure stress was reached in the simulated specimen, the magnitude of the maximum axial stress and the cross-sectional area at its location in the specimen were extracted. In addition to these values, the average gage section axial stress and its cross-sectional area were extracted as well. The important consideration is how the stress concentration is behaving right at the onset of failure, since its behavior at this point will influence the performance of the specimen. So, throughout the remainder of this study, results are assumed to have been taken right at the onset of failure based on each configuration's experimentally derived compressive strength—that is, the maximum axial stress at the onset of failure during a physical compression test.

2.3 Model Validation (Study 0)

After successful generation of the baseline model and completion of the simulation, a comparison to similar FEA simulation results observed in Dunlay[8] was performed as a validation test. Four critical points of the various maximum stress locations were noted in Dunlay[8] and are presented again in Fig. 3.

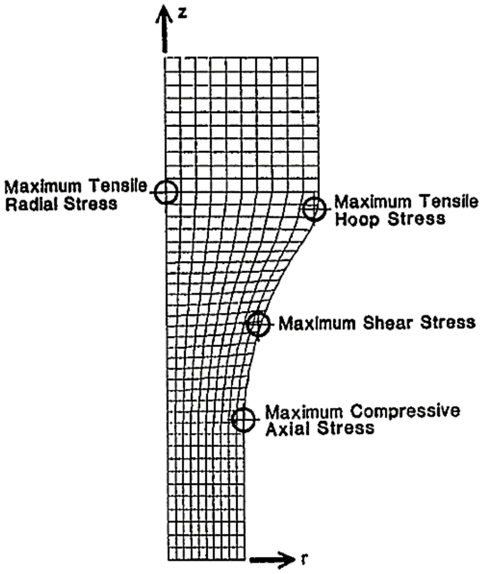

Fig. 3 Schematic of the model used in Dunlay et al.[8] with the four highlighted critical stress points. The locations (and magnitudes) of these points will be compared to the baseline model generated for this study as part of the validation procedure.

Matching the locations of these critical stresses and comparing the various stress and strain distribution plots presented in that work are the metrics by which the current model will be evaluated and, hopefully, validated. The first comparison, and potentially the most important, is axial stress distributions (Fig. 4).

As discussed in Dunlay[8], an area of particular interest in these specimens is the transitional region between the gage section and first fillet, where the maximum axial (compressive) stress contour can be seen in both plots in Fig. 4. The current simulation also confirms this critical stress location with Fig. 3. The maximum axial stress in the literature specimen at failure was 3.95 GPa while the gage section only exhibited an average axial stress of 3.59 GPa.[8] This disparity yields a 10% increase in stress between the stress concentration and the gage section. Similarly, the baseline specimen used in this study experienced an increase in stress of 9.4% between average gage section stress and the point of maximum stress.

By comparing the (A) and (B) plots of the literature model and the baseline configuration (Figs. 4–7), it is easy to observe that the current model matches the historical model to a high degree, including locations of the critical stress points.

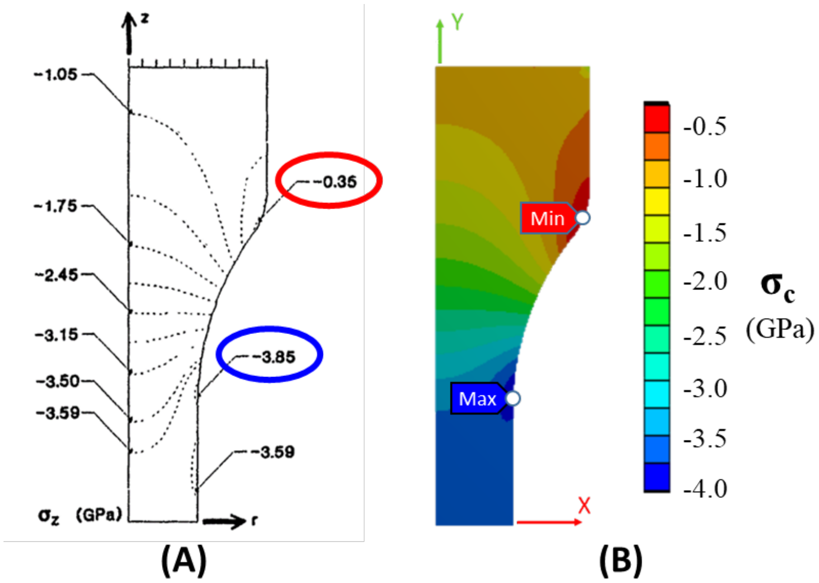

Fig. 4 **Stress contour plots of the axial (compressive) stress components for A) the literature specimen from Dunlay et al.[8] and B) the baseline configuration. Maximum compressive stress values are denoted in blue, while minimum values are denoted in red.**

To further validate that the current model predicts the same results as the literature study, the stress contours were plotted for shear and principal stresses. Again, the figures align closely with the figures generated by Dunlay[8]—the magnitudes and profiles of the regions for respective plots of shear and principal stresses are quite similar.

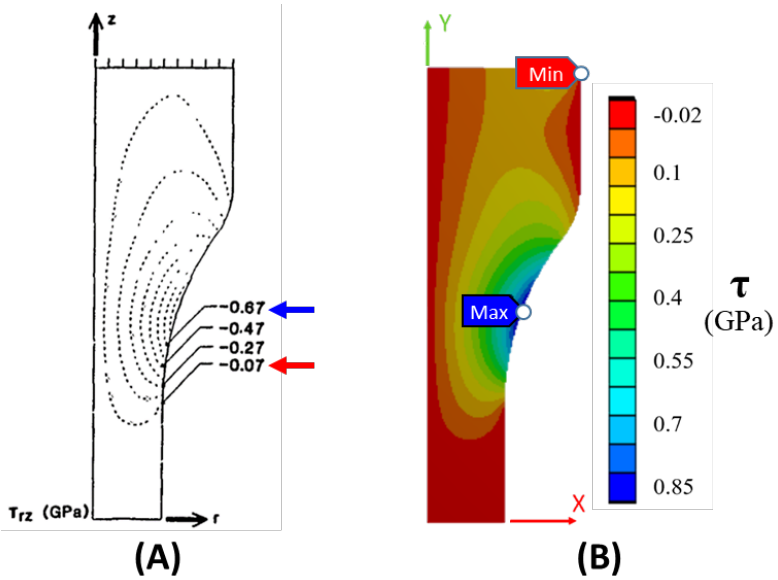

Fig. 5 **Stress contour plots of the shear stress components for A) the literature specimen from Dunlay et al.[8] and B) the baseline configuration. The contours of maximum (blue) and minimum shear stress values (red) are noted. The baseline agrees with the critical point for maximum shear stress in Fig. 3.**

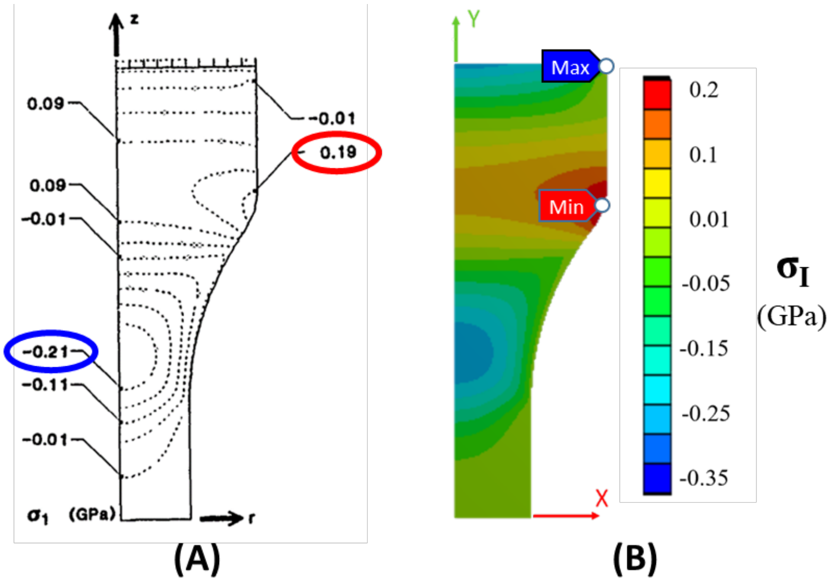

Fig. 6 Stress contour plots of the maximum (first) principal stresses for A) the literature specimen from Dunlay et al.[8] and B) the baseline configuration. The contours of maximum (blue) and minimum first principal stress values (red) are noted.

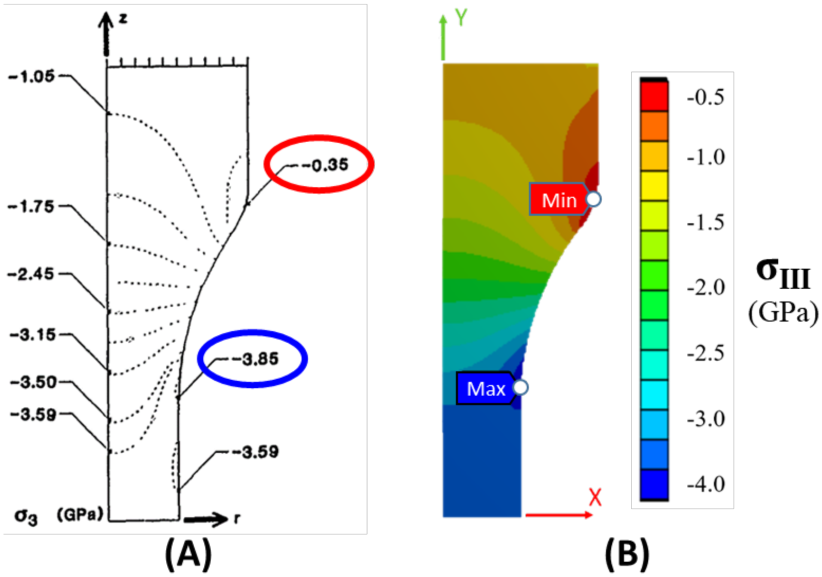

Fig. 7 Stress contour plots of the minimum (third) principal stresses for A) the literature specimen from Dunlay et al.[8] and B) the baseline configuration. The contours of maximum (blue) and minimum third principal stress values (red) are noted.

2.4 Comparison to Cuboidal and Cylindrical Specimens

Before moving onto the five studies, it was determined that a comparison of dumbbell-shaped specimens needed to be drawn in relation to typical cuboidal and cylindrical compression specimen geometries. These conventional specimen geometries have previously been investigated in a variety of different sizes and geometries; however, representative geometries have been selected for this current study. It is anticipated that similar geometries (not modeled here) would not greatly affect the outcomes. A cuboidal specimen commonly used for testing of advanced ceramics[17–21] was modeled with dimensions of 3.5 by 4.0 by 5.3 mm^3 (height by width by length). This specimen is presented in Fig. 8a. Note that for the purposes of comparison, the cuboid specimen was modeled using a 2D plane-stress approximation to improve the mesh resolution and simulation times. (A brief comparison was made with the 3D model, and results were very similar, hence validating the plane stress approximation.) A cylindrical specimen used for standardized compression strength testing of whiteware ceramics[22] was also modeled with a radius of 3.18 mm and a total length of 12.7 mm (Fig. 8b).

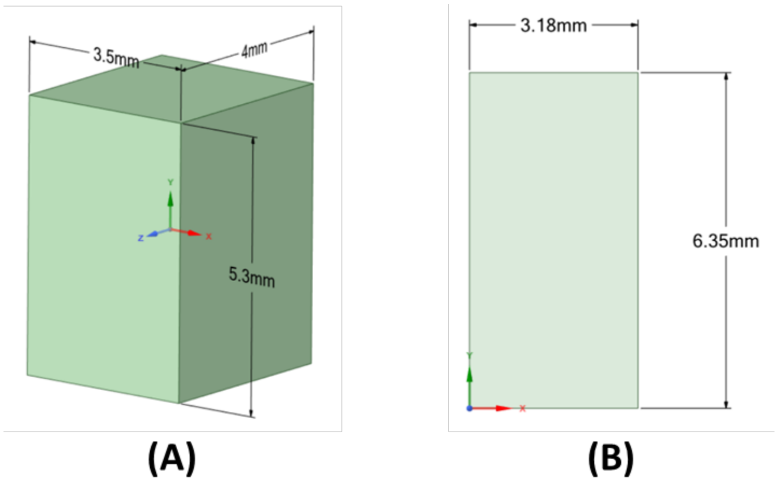

Fig. 8 Specimen geometries for the A) cuboid (3D) and B) cylindrical (2D axisymmetric) generated for simulation with the current model and comparison to the baseline dumbbell geometry

Aside from the obvious geometric differences, these specimens were simulated identically to that of the baseline configuration. No distinct gage section exists for these specimens because the cross section is constant along the y-direction, so a region within the center of both specimens, approximately one-quarter of the total specimen length (black dashed area in Fig. 9), was chosen to represent the average gage section stress.

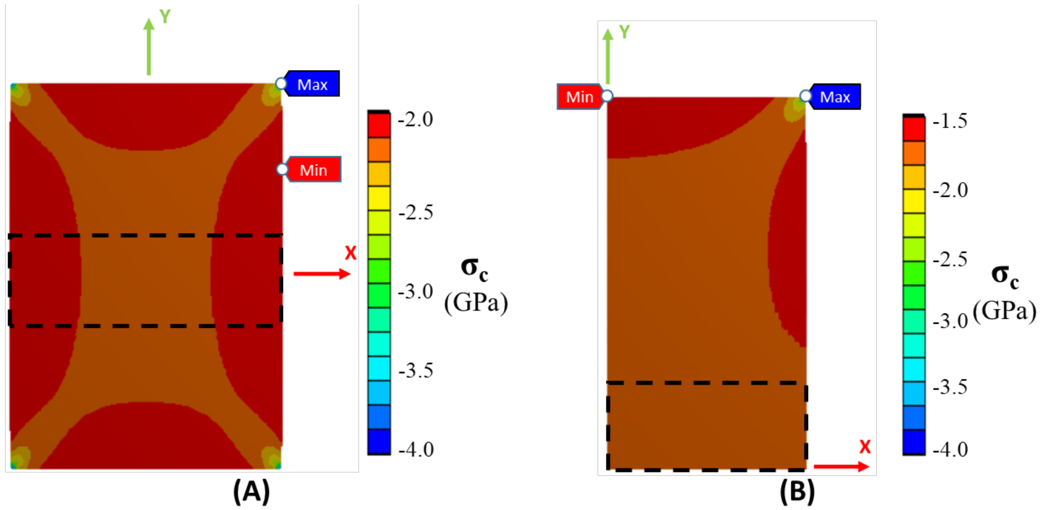

Fig. 9 Plots of the stress contours for the A) cuboid (plane-stress 2D view) and B) cylindrical specimens. The dashed black outline is the portion considered for the gage section and is approximately one-quarter of specimen length. The average stress across this region was taken as the gage section compressive stress value.

The cuboidal specimen had an 80% increase in stress between the gage section and stress concentration (which occurred along the edges of both specimens), while the cylindrical specimen had a 122% increase in stress between these points. When compared to the performance of cylindrical or cuboidal specimens, dumbbell specimens drastically minimize the percent difference in stress between the gage section and the point of maximum stress. The reduction in percent difference of stress through using dumbbell specimens is clear; however, stress concentrations still exist in these dumbbell specimens, which continue to influence the compressive strength material performance.

3. Results

In order to compare the output for the various configurations within each study, contour maps of axial stress and strain were generated along with values of the cross-sectional area of both the stress concentration and the gage section at the time of failure. Thus, alterations to the specimen size-scale, geometry, and loading conditions were made in an attempt to understand the dominant parameters for compression testing of ceramic dumbbell specimens; this was done to minimize the differences in compressive stress and cross-sectional area between the gage section and the maximum stress concentration point.

3.1 Study 1: Specimen Down-Scaling

One aspect of compression testing ceramics that is important is the physical size of the specimen. Producing large plates or billets of ceramics is a nontrivial task, hence why small specimen sizes are typically employed for mechanical testing. It is desired to extract specimens from the typical manufacturing process used to make ceramic armor plates (typically <1 inch thick) to ensure that test specimens are representative of the full-scale component's microstructure. Therefore, scaled-down versions of the baseline specimen were chosen for simulations to determine if there is a size-scale effect on the compression strength of these dumbbell specimens. The largest of these scaled-down specimens is 12.7 mm (0.5 inch) long (Fig. 10), which can be extracted from a typical ceramic armor plate.

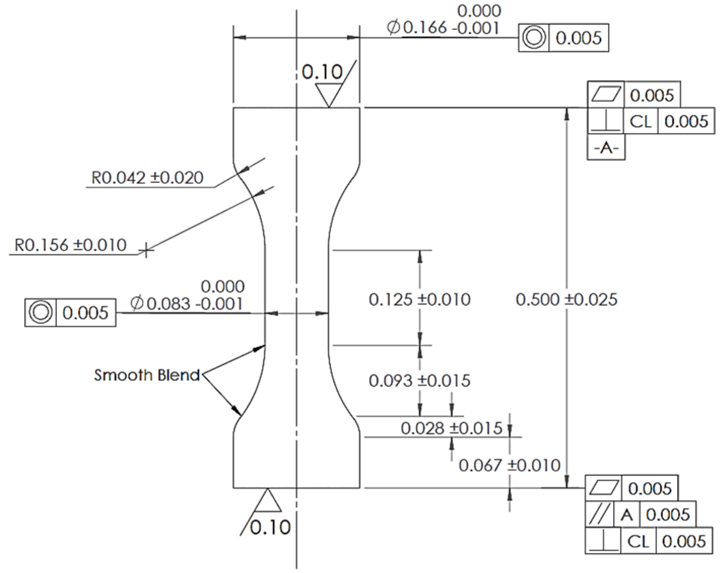

Fig. 10 Detailed drawing of Configuration A geometry (inches). This specimen geometry is designed to be easily extracted from conventional ceramic armor plate geometries.

In an effort to bridge the gap to micromechanical test specimens, two further scaled-down versions of this specimen were also investigated at one-half and one-quarter scale (i.e., 6.35- and 3.675-mm specimen lengths, respectively). The overall specimen length and associated gage length for the three specimens are presented in Table 2.

Table 2 **Configurations A, B, and C specific input parameters as varied from the baseline**

Configuration	Geometry: lengths (mm)	
	Specimen	Gage section
A	12.7	3.18
B	6.35	1.57
C	3.18	0.79

Scaling the specimen's overall size did not affect the stress contours or magnitudes—it solely affected the amount of time needed for stress and strain values within the gage section to reach critical values. In fact, almost every specimen's contour maps for QS testing were quite similar to that of the baseline (they are thus not presented). The fact that the time to failure changes proportionally to specimen scale is expected since length and area are inversely proportional to strain and stress, respectively. As deformation increases during compression, the critical strain will be reached faster if the length of the undeformed specimen is decreased (per the equation for axial strain). Configuration A had a stress concentration that was 9.5% higher than the gage stress at a point where the cross-sectional area was 1.1% larger than the gage section area. Similarly, Configurations B and C both exhibited an increase of 9.5% and 0.8% in stress and area, respectively. All of these stress concentrations were at the same point—the transition from the first fillet into the gage section—which was the same point noted in Fig. 3. Compared with the baseline specimen, which is 30.5 mm long, the maximum stress conditions only vary slightly to that of Configurations A–C. The small variation could be attributed to slight geometrical differences noticed between the baseline specimen and Configuration A (Configuration A is not a perfectly scaled-down version of the baseline), and also because the simulation is stopped when the critical failure stress value is reached, which may occur at slightly different "scaled" times due to the timesteps being the same for both simulations. Hence, it can be concluded that scaling the specimen changes the stress distribution by negligible amounts. However, this assumption does not consider microstructural variations in the flaw distribution of a smaller specimen, which are not implemented in this model and may influence the failure behavior. This issue will be discussed in greater detail later in the investigation. Nevertheless, in light of the comparable stress distributions and greater affinity for the smaller specimen size of Configuration A for future testing, the subsequent studies will compare their results with Configuration A rather than the larger baseline specimen (equivalent to the B specimen detailed in Dunlay et al.[8]) described in Study 0.

3.2 Study 2: Displacement Rate

Changing the displacement rate of the QS compression test proved to have an inversely proportional effect on the time to failure. Configuration D was compressed at half the rate of Configuration A (Table 3), hence critical values of strain were not reached until it was compressed to the same amount, which took twice as long. Configuration D failed at 19.0 s instead of the original 9.5 s seen in Configuration A. The percent increase in stress between the gage section and the stress concentration was 9.6%, and the cross-sectional area at this point was 0.8% larger than the gage section. These values are consistent with Configuration A as the only variation in the output was the doubling of time to failure.

Table 3 Configuration D specific input parameters as varied from the baseline

Configuration	Displacement rate (mm/min)
D	0.25

3.3 Study 3: Specimen Geometry

In an effort to perform a rudimentary sensitivity study of the dumbbell specimen geometry, a few basic geometric modifications were investigated as possible improvements. Initially, the gage section length of 3.18 mm was modified by ±0.43 mm (Configurations E and F, respectively) without changing the fillet sizes. Next, modifications to the two fillets were examined: extending the second fillet to the end of the specimen (Configuration G) and maximizing the radius of the first fillet (Configuration H). Finally, a small chamfer was placed at the edge of the specimen end cap to reduce the likelihood of premature failure due to the stress concentration at that point (Configuration I). These geometry modifications are summarized in Table 4.

Table 4 Configurations E, F, G, H, and I specific input parameters as varied from the baseline

Configuration	Gage length (mm)	Geometry modification
E	3.61	Lengthened gage section
F	2.74	Shortened gage section
G	1.27	Shortened gage section with second fillet extended to end (i.e., no cylindrical end cap)
H	1.27	Shortened gage section with maximum first fillet radius allowing to maintain cylindrical end cap
I	3.18	Chamfer on end cap edge

Lengthening the gage section, and thereby decreasing the radius of the first fillet, slightly increased the percent difference between maximum stress and average gage stress (Configuration E). Conversely, shortening the gage section, and thereby increasing the radius of the first fillet, proved to slightly decrease this percentage (Configuration F). The maximum stress in Configuration E was 11.2% higher than the average gage section stress, while the maximum stress in Configuration F was 8.3% higher than the average gage section stress. This indicates that specimens with shorter gage lengths are less sensitive to changes in area as one moves along the specimen length because the radius of the first fillet is larger, and the tangential slope into the gage section is less severe. Hence, a specimen with a shorter gage section should produce smaller changes in area between the point of maximum stress and the gage section stress than a longer gage section. This relationship is noticed in Configurations E and F, where the percent difference in cross-sectional area from gage to the maximum stress location is 1.5% and 0.2%, respectively. However, a reduced gage length provides a smaller volume for failure to occur in; therefore, an optimum balance must be determined.

In a further effort to reduce the difference between the point of stress concentration and the gage section stress, two geometry modifications were created (Configurations G and H). The aim of these specimens was to further decrease the length of the gage section and increase the radius of the first fillet, resulting in the smoother transition into the gage section mentioned previously. The overall width and length of these newly designed dumbbell specimens were held constant to that of the baseline geometry; however, the gage section length was shortened to 1.27 mm, and the two fillets connecting the gage section to the end caps were maximized. In Configuration G, the second fillet extends the entire way to the specimen's end (Fig. 11a), which is different from the baseline design where a 1.70-mm cylindrical end cap is present. Configuration H, on the other hand, includes this 1.70-mm cylindrical end cap but increases the radius of the second fillet to maintain the radius of the maximized first fillet (Fig. 11b).

The percent increase from average gage section stress to the point of maximum compressive stress is 6.2% and 6.3% for Configurations G and H, respectively, and the percent difference in cross-sectional area for these two points is about 0.6% and 0.4%, respectively. These values are improvements from the 9.5% and 1.1% increase in stress concentration and cross-sectional area at that point, respectively, for Configuration A.

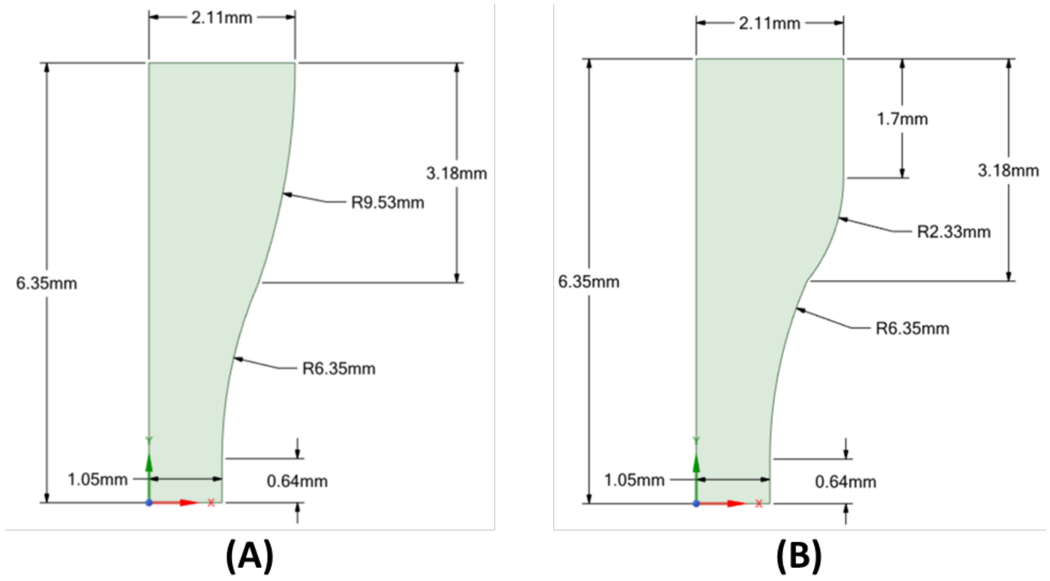

Fig. 11 Modified dumbbell geometries of A) Configuration G and B) Configuration H. The first fillet radius is maximized in both conditions. However, in Configuration G, the second fillet extends to the end of the dumbbell, negating the end cap in the baseline geometry. In Configuration H, the end cap from the baseline geometry is maintained, but the second fillet radius is maximized.

In an effort to visualize the trend of reduced gage length decreasing the stress concentration point, a plot was created of gage section length to the percent increase between average gage stress and stress concentration point (Fig. 12). Generally, as the gage section length is increased, the percent difference in stress between the gage section and the stress concentration point also increases. The B specimen from Dunlay[8] is also plotted to help correlate the two functions. For each specimen, data was collected when about 4 GPa of compressive stress was reached in the specimen; however, because of how ANSYS generates discretized data, these stress values can vary by ±50 MPa. Between similar tests of any given configuration, results for percent increase in stress at the concentration point varied by approximately 0.25%; therefore, error bars denoting this degree of error were generated on the individual data points.

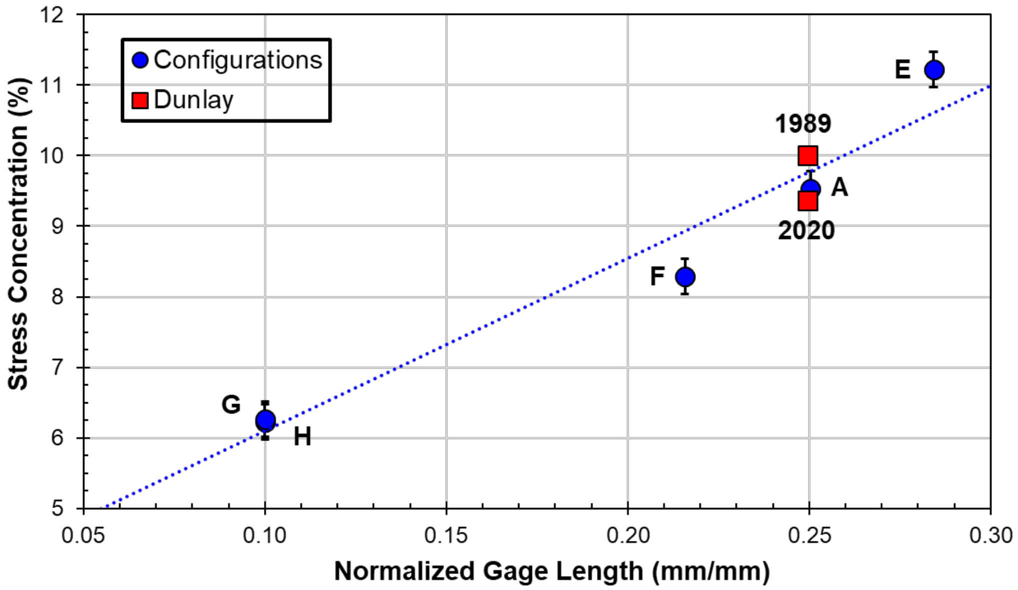

Fig. 12 Plot of percent increase in stress at the concentration point vs. normalized gage length for Configurations A, E, F, G, and H (blue) compared to the "B" specimens (red) from Dunlay et al.[8] (1989) and the baseline specimen in this study (2020). The gage lengths have been normalized to the total specimen length.

As seen in Fig. 4, a stress concentration is also noticed on the outer edge of each specimen's end cap—a concentration similar to the one seen in the cylindrical specimen (Fig. 9b). If this concentration reaches a critical value early in the loading process, it could cause extremely premature failure and invalidate any experimental results. In an attempt to minimize this concentration, a chamfer with 0.25-mm width and height was added to the edge of Configuration A. This modification is considered Configuration I and can be seen in Fig. 13.

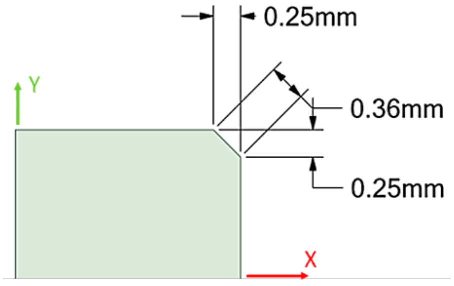

Fig. 13 Detailed drawing of the edge chamfer modification to the geometry used for Configuration I to attempt to reduce the interfacial stress concentration at this point in the geometry of Configuration A

Configuration I was then simulated in ANSYS to observe the new behavior during compression testing. The stress contour plots for both Configuration A (Fig. 14a) and Configuration I (Fig. 14b) at the onset of failure are presented.

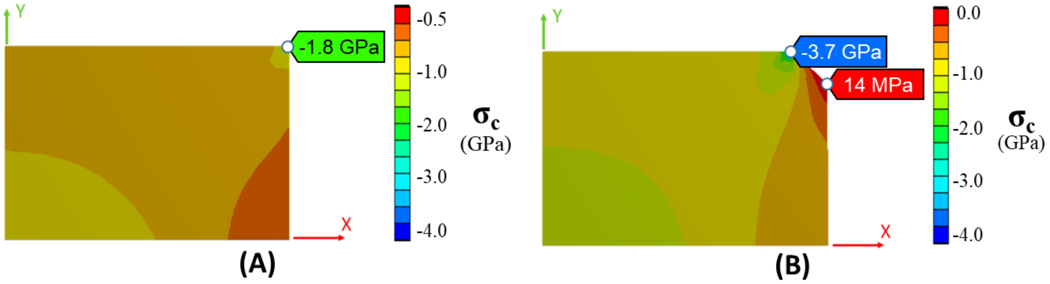

Fig. 14 Axial stress contour plots for A) Configuration A and B) Configuration I with the added edge chamfer

Unfortunately, the new chamfer had an adverse effect, effectively doubling the magnitude of the stress concentration to 3.7 GPa, rather than the 1.8 GPa seen in Configuration A. This indicates that a chamfer in this area is not ideal for stress reduction. A tensile stress concentration of magnitude 14 MPa is noticed on Configuration I as well, which may further complicate the design. Further testing is necessary to determine how to best minimize this edge stress concentration.

3.4 Study 4: Boundary Conditions

In physical testing of dumbbell specimens, cylindrical WC inserts are often used between the specimen and loading platen to reduce indentation and lateral effects.[8,11,15,23,24] The historical model incorporated WC inserts that were half-dumbbell shaped and radius-matched to the end of the ceramic dumbbell specimen.[8] However, a platen of this geometry does not appear to be requisite, and they are expensive to machine. More commonly, WC cylinders are used as platens. To test how a cylindrical WC insert would affect the performance of dumbbell specimens, two simulations were run of a 6.35-mm-thick WC cylinder with two different radii (Table 5): one matched to the specimen end caps and another that overhung the edges of the specimen.

Table 5 Configurations J, K, and L specific input parameters as varied from the baseline

Configuration	Loading modification
J	Radius-matched WC insert (i.e., flush)
K	Large-radius WC inserts (i.e., overhanging)
L	Frictionless upper support

For Configuration J, the WC platen was radius-matched to the specimen end cap (i.e., flush); while in the second simulation, Configuration K, the WC insert extended beyond the dumbbell end cap by one radius (i.e., overhanging). The compressive stress contour maps for each test can be seen in Fig. 15.

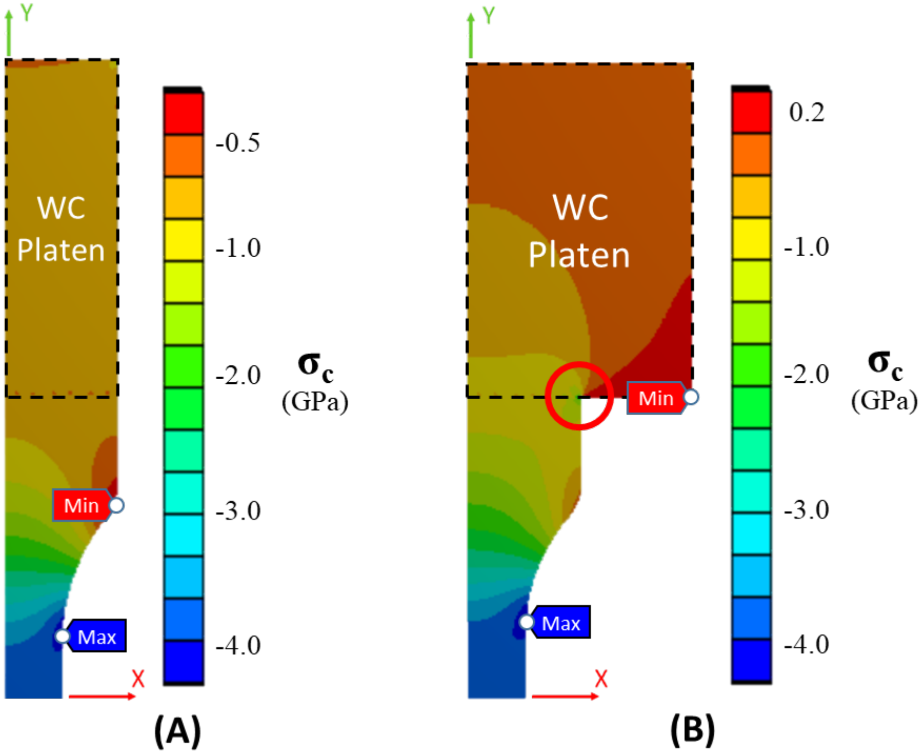

Fig. 15 Detailed view of the stress contour plots of the axial (compressive) stress component for A) Configuration J (flush WC platen) and B) Configuration K (overhanging WC platen). A dotted black line has been added to denote the boundary of the WC platen.

While the percent difference in stress and area at the concentration point compared to the gage section is similar to that of Configuration A, Configurations J and K have dissimilar stress contour maps. Configuration J exhibits an approximately homogenous stress distribution on this outer region, including omission of the stress concentration at the specimen edge noted in Configuration A. On the other hand, a stress concentration is now noticed on the outer edge of Configuration K (seen within the red circle), where the alumina specimen appears to be "indenting" the WC. The overhang induces a nonuniform loading distribution on the top edge of the specimen while the platen is also deforming elastically around the specimen end cap, which promotes bending and shearing stresses (i.e., triaxial loading). While Configuration K may fail because of this stress concentration, having a magnitude of 2.3 GPa (0.5 GPa greater than Configuration A) at the moment of failure, its gage section and maximum stress conditions are minimally affected. The percent increase from average gage section compressive stress to maximum compressive stress is about 9.4% for both Configurations J and K, and the percent difference in area is about 0.9% and 0.2%, respectively, at the onset of failure.

The effect of friction on the loading surface was also investigated. Previously, a displacement support of infinite friction was placed on the top of the specimen, where movement in the x-direction was restricted, as indicated by the results of Dunlay.[8] Conversely, Configuration L simulates a frictionless interface during compression testing (Table 5). While the values for percent increase in stress and area between gage and stress concentration point are similar to that of Configuration A, the stress distributions in the contour plot have changed slightly (Fig. 16).

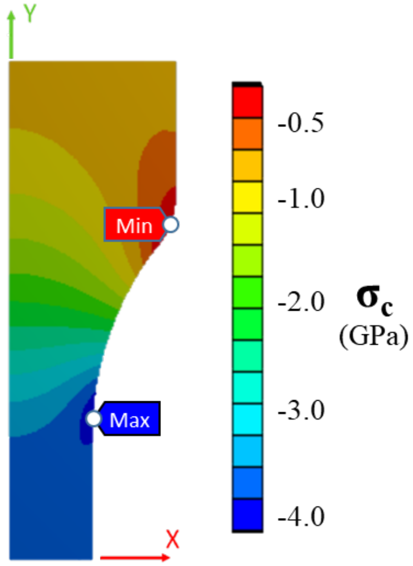

Fig. 16 Stress contour plot of the axial (compressive) stress component for Configuration L with a frictionless loading interface

The interior region of the specimen (i.e., closer to central axis) exhibits a slightly larger stress magnitude than previously observed in Fig. 4 (infinite friction). The stress concentration at the edge of the specimen is no longer apparent as well. The way this specimen distributes stress through the end cap and into the gage section could change specimen performance; if stress concentrations are minimized within the end cap, failure is more likely to occur within the gage section. Configuration L experienced a 9.6% increase in compressive stress between the gage section and the maximum stress point—slightly higher than that of Configuration A. In physical testing, interface behavior is expected to be closer to that of Configuration L, a frictionless support, rather than Configuration A, which assumes infinite friction at the interface, since lubrication and precision-machined inserts are often used. However, in general, the results will fall somewhere between the two because ideal conditions are extremely difficult, if not impossible, to obtain.

3.5 Study 5: High-Rate Loading

Advanced ceramics, such as alumina, are known to exhibit strain-rate sensitive response.[10,15,25–27] Therefore, acquiring the high-rate, or dynamic, properties of these materials is of the utmost importance, especially when considering armor-grade ceramics are employed in ballistic impact situations. To this point, simulating the high-rate response of the dumbbell-shaped compression specimen is an important consideration for this study to determine if high-rate loading has an influence on the outcome.

To accomplish this, a ramp-like displacement profile was imposed on the Configuration M specimen over a span of 250 µs. Approximately 50 µs into testing, an axial stress of 4.9 GPa was reached at the location of maximum stress (Fig. 17). At this point, the axial stress in the gage section is approximately 4.5 GPa, which is comparable to the compressive strength measured during dynamic compression testing of a dumbbell specimen of the same material.[10] The top-half of the specimen deformed about 0.05 mm in this time (which correlates to 0.1 mm of deformation for the whole specimen), resulting in a strain rate of about 160 s^{-1}. This is in very good agreement with the majority of the strain rates attained in the round-robin study on the same material.[10]

The percent difference in stress and area between the point of maximum stress and the gage section was 7.5% and 0.8%, respectively. It is interesting to note that these values are slightly lower than the values for the equivalent QS test (Configuration A).

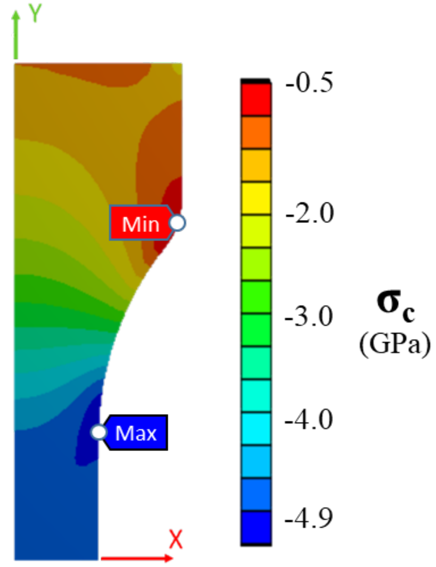

Fig. 17 Stress contour plot of the axial (compressive) stress component for the Configuration M dynamic study

4. Discussion

The results of each configuration for all five of the studies are compiled into Table 6. This table presents the overall maximum axial (compressive) stress, average gage section axial stress, cross-sectional area at the point of maximum axial stress, cross-sectional area of the gage section, and their respective percent differences at the time of failure.

Table 6 Maximum and gage section conditions of each configuration at the time of failure

Study	Config.	Max. stress (GPa)	Avg. gage stress (GPa)	% diff.	Area at max. stress (mm^2)	Gage area (mm^2)	% diff.
0	Original	3.95	3.59	10.0	…	…	…
	Baseline	3.97	3.63	9.36	20.6	20.2	1.98
1	A	4.00	3.65	9.53	3.53	3.49	1.14
	B	4.00	3.65	9.50	0.91	0.90	0.75
	C	4.00	3.65	9.54	0.23	0.23	0.75
2	D	4.00	3.65	9.58	3.52	3.49	0.76
3	E	3.95	3.55	11.2	3.63	3.58	1.51
	F	4.01	3.70	8.29	3.62	3.62	0.19
	G	3.93	3.70	6.22	3.64	3.62	0.56
	H	3.97	3.74	6.27	3.64	3.62	0.37
	I	3.95	3.61	9.34	3.63	3.62	0.37
4	J	3.96	3.62	9.43	3.54	3.50	0.95
	K	4.00	3.65	9.38	3.73	3.72	0.18
	L	3.98	3.63	9.63	3.54	3.50	1.14
5	M	4.88	4.54	7.53	3.54	3.51	0.76

Each configuration whose stress and strain contour map were not shown exhibited similar behavior and distribution to that of Configuration A (seen in Figs. 3 and 4). Table 6 shows that the parameter which most dominantly affected performance was specimen geometry, Study 3. By manipulating specimen geometry, specifically gage length, the percent increase in stress from the gage section to the point of maximum stress changed, respectively. Increasing the gage length yielded a greater difference between gage and maximum stress conditions, while decreasing gage length yielded a smaller percent difference. Modifying the shape and proportions of both fillets on the dumbbell changed these results as well. The best performing configurations in terms of minimizing this percent increase in stress were Configurations G and H, both of which yielded approximately a 6.2% difference in axial stress between the gage section and the stress concentration. A thorough sensitivity study of the dumbbell specimen geometry should be conducted to further minimize these stress concentration conditions.

Studies 1, 2, and 4 aimed to change other input parameters, such as specimen size, loading rate, and boundary conditions, each of which affected the performance of the specimen, in terms of minimizing stress differences, by negligible amounts. Study 5 found that tests in higher strain-rate regimes reduced the percent difference in stress and area between the gage section and the point of maximum stress. The exact phenomenon that causes this is unknown, so additional examination is needed.

During this experiment, several assumptions were made to reduce the variability of simulation and simplify analysis. First, fracture mechanics was not considered. Fracture mechanics plays a large role in determining material performance of ceramics, so removing it from the analysis will certainly affect the results. However, the linear-elastic behavior seen in these studies provides a rudimentary understanding of how a specimen would behave when subjected to axial compression. Similar stress concentrations would be apparent even with the inclusion of fracture mechanics. Classically, fracture mechanics dictates when and how brittle materials fail; however, for the purposes of this study, where understanding the distribution of stress was paramount, fracture mechanics was not needed. This allows for simpler simulations and a more streamlined analysis.

Material microstructure is also quite important in compression testing, especially in ceramics where flaw distributions have a great effect on material performance. However, because of the limitations of the simulation software, as well as complexity of simulating real (or even simplified) material microstructure in compression testing, microstructure was not implemented and material behavior was assumed homogeneous. Further testing and simulation should be conducted to evaluate the effects of both fracture mechanics and material microstructure on specimen performance.

5. Conclusions

Dumbbell specimens in past studies have been used to determine material properties of ceramics, as proposed by Carl Tracy in the 1980s.[4] The use of dumbbell-shaped specimens is an improvement over the previous cylindrical and cuboidal geometries because they minimize stress concentrations occurring on the outer edge interface, as well as aim to promote the onset of failure in the gage section. However, new stress concentrations are noticed within the first fillet just outside of the gage section on these dumbbell specimens, which can still lead to slightly underestimated material performance. To quantify this stress concentration, the percent increase in stress and cross-sectional area between the gage section and the stress concentration point is extracted via simulations in ANSYS. A specimen that produces a stress concentration as close in magnitude and cross-sectional area to that of the gage section will provide the most accurate values of material properties during physical testing. Initially, the dumbbell specimen proposed by Tracy[4] and Dunlay et al.[8] was recreated and analyzed to validate the current model and obtain baseline values. Then, to determine which parameters had the greatest effect on the specimen's stress concentration, several input parameters were modified and results were obtained. These modifications were broken down into five studies in which size scale, loading rate, geometry, and boundary conditions were all varied. The parameter that affected the percent difference in stress between the gage and concentration point the most was specimen geometry, Study 3. Specifically, reducing the overall length of the gage section and enlarging the first fillet radius reduced the percent increase in stress by almost 3.3% when compared to the results of Configuration A. We predict this percent increase in stress can continue to be reduced by enhancing dumbbell specimen geometry, which requires further thorough analysis and simulation. Therefore, an emphasis on perfecting dumbbell specimen geometry instead of other input parameters, as studied in this report, should be made to obtain the most accurate measurements of material properties when conducting physical compression tests.

6. References

1. Sines G, Adams M. Compression testing of ceramics, in flaws and testing. Boston (MA): Springer; 1978. p. 403–434.
2. Rudnick A, Marscall CW, Duckworth WH. The evaluation and interpretation of mechanical properties of brittle materials. Columbus (OH): Battelle Memorial Inst., Defense Ceramic Information Center; 1968.
3. Adams M, Sines G. Methods for determining the strength of brittle materials in compressive stress states. Journal of Testing and Evaluation. 1976;4(6):383–396.
4. Tracy CA. A compression test for high strength ceramics. Journal of Testing and Evaluation. 1987;15(1):14–19.
5. Tracy C, Slavin M, Viechnicki D. Ceramic fracture during ballistic impact. Advances in Ceramics: Fractography of Glasses and Ceramics. 1988;22:295–306.
6. Birch JM, Wilshire B, Owen DJR, Shantaram D. The influence of stress distribution on the deformation and fracture behaviour of ceramic materials under compression creep conditions. Journal of Materials Science. 1976;11(10):1817–1825.
7. Bortz SA, Burton KT. Analysis and review of mechanical testing procedures for brittle materials. Chicago (IL): IIT Research Institute; 1968.
8. Dunlay WA, Tracy CA, Perrone PJ. A proposed uniaxial compression test for high-strength ceramics. Watertown (MA): Army Materials and Mechanics Research Center; 1989.
9. Swab JJ, Meredith CS, Casem DT, Gamble WR. Static and dynamic compression strength of hot-pressed boron carbide using a dumbbell-shaped specimen. Journal of Materials Science. 2017;52(17):10073–10084.
10. Swab JJ, Quinn GD. Dynamic compression strength of ceramics: results from an interlaboratory round-robin exercise. Aberdeen Proving Ground (MD): CCDC Army Research Laboratory; 2019 Nov. Report No.: ARL-TR-8860.
11. Chen W, Subhash G, Ravichandran G. Evaluation of ceramic specimen geometries used in a split Hopkinson pressure bar. Dymat Journal. 1994;1(3):193–210.

12. Blumenthal W, Gray G, Claytor T. Response of aluminium-infiltrated boron carbide cermets to shock wave loading. Journal of Materials Science. 1994;29(17):4567–4576.

13. Blumenthal WR. High strain rate compression testing of ceramics and ceramic composites. Advances in Ceramic Armor: A Collection of Papers Presented at the 29th International Conference on Advanced Ceramics and Composites; 2005 Jan 23–28; Cocoa Beach, FL. 2005. John Wiley & Sons.

14. Pickup I. The correlation of microstructural and mechanical characteristics of silicon carbide with ballistic performance. Advances in Ceramic Armor: A Collection of Papers Presented at the 29th International Conference on Advanced Ceramics and Composites; 2005 Jan 23–28; Cocoa Beach, FL. 2005. John Wiley & Sons.

15. Cosculluela A, Cagnoux J, Collombet F. Uniaxial compression of alumina: structure, microstructure and strain rate. Le Journal de Physique IV. 1991;01(C3):C3-109–C3-116.

16. CoorsTek. Cerashield and cercom armor ceramics for superior lightweight protection. Golden (CO): CoorsTek; 2017.

17. Hogan JD, Farbaniec L, Sano T, Shaeffer M, Ramesh KT. The effects of defects on the uniaxial compressive strength and failure of an advanced ceramic. Acta Materialia. 2016;102:263–272.

18. Hu G, Ramesh KT, Cao B, McCauley JW. The compressive failure of aluminum nitride considered as a model advanced ceramic. Journal of the Mechanics and Physics of Solids. 2011;59(5):1076–1093.

19. Farbaniec L, Hogan JD, Ramesh KT. Micromechanisms associated with the dynamic compressive failure of hot-pressed boron carbide. Scripta Materialia. 2015;106:52–56.

20. Hogan JD, Farbaniec L, Shaeffer M, Ramesh KT. The effects of microstructure and confinement on the compressive fragmentation of an advanced ceramic. Journal of the American Ceramic Society. 2015;98(3):902–912.

21. Hogan JD, Farbaniec L, Daphalapurkar N, Ramesh KT. On compressive brittle fragmentation. Journal of the American Ceramic Society. 2016;99(6):2159–2169.

22. ASTM C773-88. Standard test method for compressive (crushing) strength of fired whiteware materials. West Conshohocken (PA): ASTM International; 2016.

23. Subhash G, Nemat-Nasser S. Dynamic stress-induced transformation and texture formation in uniaxial compression of zirconia ceramics. Journal of the American Ceramic Society. 1993;76(1):153–165.

24. Subhash G, Nemat-Nasser S. Uniaxial stress behaviour of Y-TZP. Journal of Materials Science. 1993;28(21):5949–5952.

25. Luo H, Chen W. Dynamic compressive response of intact and damaged AD995 alumina. International Journal of Applied Ceramic Technology. 2004;1(3):254–260.

26. Lankford J. Mechanisms responsible for strain-rate-dependent compressive strength in ceramic materials. Journal of the American Ceramic Society. 1981;64(2):C-33–C-34.

27. Jiao T, Yulong L, Ramesh KT, Wereszczat AA. High rate response and dynamic failure of structural ceramics. International Journal of Applied Ceramic Technology. 2004;1(3):243–253.

List of Symbols, Abbreviations, and Acronyms

2D	two-dimensional
3D	three-dimensional
FEA	finite element analysis
QS	quasi-static
WC	tungsten carbide

1 (PDF)	DEFENSE TECHNICAL INFORMATION CTR DTIC OCA
1 (PDF)	CCDC ARL FCDD RLD CL TECH LIB
1 (PDF)	CCDC ARL FCDD RLW MB J PITTARI